Int. J. Anal. Appl. (2026), 24:374

International Journal of Analysis and Applications

Fractional Brusselator Modeling for Hydrothermal Mining Applications

A. M. Shloof[1], Mohamed I. Nouh[2], Abaker A. Hassaballa[3,*], Halema Ali Hamead[4]

[1]*Department of Mathematics, Faculty of Science, University of Zintan, AlZintan, Libya*
[2]*Department of Astronomy, National Research Institute of Astronomy and Geophysics, 11421 Helwan, Cairo, Egypt*
[3]*Center for Scientific Research and Entrepreneurship, Northern Border University, Arar, 73213, Saudi Arabia*
[4]*Department of Mathematics, Faculty of Education, University of Aljufra, Aljufra, Libya*

[*]*Corresponding author:* Abakerh@gmail.com

Abstract. This study unifies verified numerical analysis of the generalized-Caputo fractional Brusselator with a new application to oscillatory mineral precipitation and reactive transport in hydrothermal ore systems. The identity $\tau = t^{\rho}/\rho$ proves that ρ is an exact clock transformation, whereas α controls memory and fractional stability. For the homogeneous model, a shifted-Legendre collocation method and a singularity-adapted basis are assessed against Runge–Kutta, fractional Adams, and implicit L1 calculations. In the integer-order benchmark, the degree-16 collocation error is 6.9×10^{-13}; for fractional solutions, endpoint enrichment improves accuracy by factors up to 325 at degree 16. The application model interprets the Brusselator variables as effective metal-bearing and ligand/redox reactants, adds a threshold precipitation variable, and couples mineral accumulation to porosity and permeability. A fractional Adams method with second-order spatial differences predicts localized, temporally modulated deposition. Reducing α from 1.00 to 0.70 lowers the final mean precipitate from 0.2199 to 0.1127, while increasing B from 1.6 to 2.8 raises the mean precipitate from approximately 2×10^{-5} to 0.2655 and produces a maximum permeability loss of 37.9%. Grid refinement stabilizes the mean precipitate to within 0.05%. The combined framework links mathematical verification to a transparent geophysical hypothesis model while explicitly distinguishing conceptual results from field-calibrated prediction.

1. Introduction

Hydrothermal ore formation is governed by the transport of hot, metal-bearing fluids through fractures and permeable rock, followed by chemical destabilization and mineral precipitation.

Received: Sep. 9, 2026.

2020 *Mathematics Subject Classification.* 26A33; 35Q86; 76V99.

Key words and phrases. fractional Brusselator; generalized Caputo derivative; shifted-Legendre collocation; hydrothermal ore systems; mineral precipitation; reactive transport; porosity–permeability feedback; mining geophysics.

https://doi.org/10.28924/2291-8639-24-2026-374
ISSN: 2291-8639

© 2026 the author(s).

Mixing, cooling, pressure changes, redox reactions, and fluid–rock interaction can localize mineral deposition. Because precipitation modifies pore space and fracture transmissivity, transport and reaction are mutually coupled rather than sequential processes [1–4]. Modern pore- and fracture-scale studies demonstrate that mineral deposition can reorganize flow paths and reduce connectivity, motivating reduced models that isolate the feedback mechanisms [2–4].

Transport in fractured and heterogeneous geological media is often non-Fickian. Broad residence-time distributions, matrix diffusion, channeling, and trapping produce early arrivals or power-law tails that are poorly represented by a single local timescale [5–7]. Fractional derivatives provide one continuum description of such memory. They do not identify a unique pore-scale mechanism by themselves; their order must ultimately be inferred from breakthrough, tracer, or reaction-progress data.

The Brusselator is a canonical nonlinear model of a driven autocatalytic reaction. It was introduced to analyze dissipative structures and symmetry-breaking instabilities [8]. Its compact kinetics exhibit a steady state, a Hopf threshold, oscillations, and—after adding spatial transport—pattern-forming behavior. These qualities make it useful as a reduced model for testing whether nonlinear chemical feedback and anomalous transport can generate oscillatory mineral deposition. The Brusselator is not itself a mineral-equilibrium model, and its variables cannot be equated with named aqueous species without calibration.

Hydrothermal mineral systems are particularly suitable for this type of reduced-order analysis because several feedback operate over strongly separated scales. Fluid circulation may persist for thousands of years, whereas nucleation, surface reaction, fracturing, or local sealing may occur over much shorter intervals. Mineral precipitation can divert flow toward neighboring pathways, expose new reactive surfaces, or isolate portions of the fracture network. The resulting deposit geometry reflects not only equilibrium chemistry but also the history of transport, mixing, and pathway evolution. High-fidelity reactive-transport models can represent these processes explicitly. Still, their large parameter requirements make it difficult to identify which feedback is responsible for an observed oscillation or spatial pattern [1–4]. A compact nonlinear model is therefore valuable when used to isolate mechanisms and formulate testable hypotheses.

Oscillatory and rhythmic mineral textures provide further motivation. Repeated bands, compositional zoning, and episodic vein growth are commonly interpreted in terms of fluctuating fluid input, pressure cycling, temperature variation, or self-organized reaction. These explanations are not mutually exclusive. A nonlinear kinetic oscillator supplies a mathematical null model: if constant external forcing can generate repeated supersaturation pulses, then not every band necessarily requires an independently imposed environmental cycle. Conversely, failure of the autonomous model to reproduce an observed period or amplitude would indicate the need for explicit periodic forcing, fracture mechanics, or evolving boundary conditions.

The classical Brusselator contains two feed parameters and two interacting fields, making its bifurcation structure transparent. For A fixed, the homogeneous integer-order system loses stability at $B = 1 + A^2$. This analytic threshold enables a controlled separation between stable, weakly oscillatory, and strongly oscillatory regimes. When transport coefficients differ, spatial modes can also compete with homogeneous instability. The model is consequently well-suited to systematic comparisons, even though it does not replace mineral-specific mass-action kinetics.

A fractional extension is motivated by the nonlocal character of transport in heterogeneous rock. Fracture channeling, stagnant zones, repeated exchange with a low-permeability matrix, and broad distributions of residence time can all produce memory in measured breakthrough curves [5–7, 9]. A Caputo derivative summarizes this memory through an order $0 < \alpha \leq 1$. Values below unity weight the preceding trajectory through a power-law kernel and generally alter relaxation and stability. The fractional order should not be treated merely as a curve-fitting adjustment: it requires comparison with conservative-tracer data and with alternative descriptions such as multirate mass transfer or continuous-time random walks.

The generalized Caputo operator adopted here—the Caputo–Katugampola derivative [10]—introduces an additional exponent ρ. Earlier numerical treatments may interpret ρ as a second physical control, but the transformation $\tau = t^\rho/\rho$ shows that, for the definition adopted here, it exactly changes the temporal coordinate. This distinction has practical consequences for inverse modeling. Simultaneously fitting α and ρ without recognizing their different roles can produce apparent parameter sensitivity that is a relabeling of time. The present study, therefore, reports physical conclusions primarily in transformed time and illustrates the exact clock collapse separately.

The geological extension also requires an immobile mineral variable. Standard Brusselator kinetics redistribute the two mobile reaction coordinates but do not record solid accumulation. We introduce a threshold law in which precipitation occurs only when the nonlinear reaction flux exceeds a prescribed critical value. The accumulated solid reduces porosity and modifies effective transport through a normalized Kozeny–Carman relation. This closure is intentionally simple: its purpose is to reveal how chemical oscillation can be converted into persistent hydraulic change. More detailed applications should replace the threshold with saturation-index-dependent mineral kinetics and use a constitutive law appropriate to the measured pore or fracture geometry [2–4,11].

The principal research question is therefore: how do fractional memory, nonlinear kinetic forcing, and precipitation-induced clogging interact to control the amount and spatial localization of mineral deposition? Three subsidiary questions are examined. First, does reducing α suppress or delay oscillatory precipitation over a fixed observation window? Second, how does crossing the classical Brusselator threshold influence mineral accumulation and permeability loss? Third, are the integrated predictions numerically stable under refinement, and when does porosity feedback materially alter transport?

This paper provides a fractional Brusselator study around a geophysically interpretable application: (i) a one-dimensional reaction–transport formulation for a hydrothermal fracture; (ii) a threshold precipitation law; (iii) porosity–permeability feedback; (iv) fractional-order, kinetic-forcing, precipitation-rate, and feedback comparisons; (v) spatial and temporal refinement; and (vi) a strict distinction between mathematical prediction and geological interpretation.

2. Geological Interpretation and Model Scope

2.1. **Conceptual hydrothermal setting.** We consider a representative one-dimensional segment of a permeable fracture or vein selvage. The dimensionless field $u(x,t)$ represents an effective activity of a mobile metal-bearing reactant, whereas $v(x,t)$ represents an effective ligand, sulfur-bearing, or redox reactant that enables autocatalytic conversion. The immobile field $p(x,t)$ measures accumulated precipitate. These variables are lumped reaction coordinates, not direct molar concentrations of a specified mineral system. Table 1 defines the physical meaning and modeling role of each variable and parameter used in this conceptual mapping.

The intended application is hypothesis testing for three observations: episodic mineral growth, oscillatory or banded zoning, and progressive loss of fracture transmissivity. Application to a particular Cu–Au, Pb–Zn, or epithermal system would require replacing the lumped kinetics with calibrated speciation and mineral-rate laws. Table 1 makes clear that the model is intentionally reduced: u and v are effective reaction coordinates, whereas p, φ, and k/k_0 translate chemical history into mineral accumulation and hydraulic response (Section 2.2 states the corresponding calibration assumption for A and B).

Table 1. Physical interpretation of model variables and parameters.

Symbol	Interpretation	Role
u	Effective metal-bearing reactant	Mobile concentration-like field
v	Ligand/sulfur/redox reactant	Complementary nonlinear reactant
p	Immobile mineral precipitate	Records cumulative deposition
α	Memory order	Controls temporal nonlocality
ρ	Generalized clock exponent	Maps transformed to physical time
A, B	Feed and kinetic forcing	Control steady state and oscillatory tendency
D_u, D_v	Effective transport coefficients	Represent spreading along the fracture
k_p, Ω_c	Precipitation rate and threshold	Convert reaction flux to mineral
φ, k	Porosity and permeability	Provide rock-property feedback

2.2. **Assumptions.**

- Isothermal, single-phase flow is assumed over the modeled segment.
- Transport is represented by effective diffusion/dispersion; explicit advection is omitted.
- A and B are dimensionless feed controls rather than measured fluid compositions.

- Precipitation is irreversible over the simulated interval.
- Porosity loss changes transport through a permeability multiplier.
- All dynamic fields share a common Caputo order in the baseline study.

3. Fractional Reaction–Transport–Precipitation Model

3.1. **Governing equations.** For $0 < x < 1$ and $0 < t \le T$, the coupled dimensionless model is

$$D_{0+}^{(\alpha,\rho)} u = D_u \kappa(\varphi) \partial^2 u/\partial x^2 + A - (B+1)u + u^2 v, \tag{1a}$$

$$D_{0+}^{(\alpha,\rho)} v = D_v \kappa(\varphi) \partial^2 v/\partial x^2 + Bu - u^2 v, \tag{1b}$$

$$D_{0+}^{(\alpha,\rho)} p = k_p \max(u^2 v - \Omega c, 0). \tag{1c}$$

Zero-flux boundary conditions $\partial u/\partial x = \partial v/\partial x = 0$ are imposed at $x = 0$ and $x = 1$. The initial state is a small, localized perturbation of the homogeneous Brusselator equilibrium, $u_* = A$ and $v_* = B/A$, with $p = 0$. The perturbation mimics spatially heterogeneous fluid input or reactive surface availability.

3.2. **Fractional operator and exact clock transformation.**

$$D_{0+}^{(\alpha,\rho)} f(t) = \rho^\alpha/\Gamma(1-\alpha) \int_0^t s^{(\rho-1)} \left(t^\rho - s^\rho\right)^{(-\alpha)} \left[s^{(1-\rho)} f'(s)\right] ds. \tag{2}$$

Let $\tau = t^\rho/\rho$ and $f(t) = F(\tau)$. Direct substitution gives

$$D_{0+}^{(\alpha,\rho)} f(t) = {}^c D_{0+}^{\alpha} F(\tau), \tau = t^\rho/\rho. \tag{3}$$

Consequently, ρ re-times every solution but does not change its path in concentration–precipitate space. Treating α and ρ as interchangeable fitting parameters would therefore be misleading: α changes memory, whereas ρ changes the physical clock.

3.3. **Porosity and permeability feedback.**

$$\varphi(x,t) = \max\left[\varphi_0 - \chi p(x,t), \varphi_{\min}\right], \tag{4}$$

$$\kappa(\varphi) = k(\varphi)/k_0 = (\varphi/\varphi_0)^3 \left[(1-\varphi_0)/(1-\varphi)\right]^2. \tag{5}$$

Equation (5) is a normalized Kozeny–Carman closure. It is used here as a monotonic constitutive hypothesis, not as a universally valid fracture law. Different pore geometries may require empirical, power-law, or micro-continuum closures [2–4, 11].

3.4. **Homogeneous stability.** Ignoring precipitation and spatial gradients, the equilibrium is (A, B/A). The kinetic Jacobian is

$$J = \left[[B-1, A^2], [-B, -A^2]\right]. \tag{6}$$

For $\alpha = 1$, the Hopf threshold is $B = 1 + A^2$; thus, $B = 2$ for $A = 1$. For a commensurate fractional system, linear asymptotic stability requires $\left|\arg(\lambda j)\right| > \alpha\pi/2$ for every eigenvalue λ_j of J. Reducing α can stabilize modes that oscillate or grow in the integer-order model, providing an analytic basis for the damping observed below.

4. Shifted-Legendre Operational-Matrix Formulation

4.1. **Generalized-Caputo transformation and shifted-Legendre preliminaries.** The numerical construction follows standard shifted-Legendre spectral-collocation practice [12, 13] and is first stated in a form that makes the roles of the two fractional parameters explicit. Let $\tau = t^\rho/\rho$ and write $f(t) = F(\tau)$. For $0 < \alpha \le 1$, the generalized-Caputo derivative adopted in this work is exactly the ordinary Caputo derivative [14] of F with respect to τ:

$$D_{0+}^{(\alpha,\rho)} f(t) = D_{0+}^{C,\alpha} F(\tau), \qquad \tau = \frac{t^\rho}{\rho}. \tag{7}$$

Accordingly, the spectral discretization can be constructed on the transformed interval $0 \le \tau \le T$. Introducing $\xi = \tau/T$ maps this interval to $0 \le \xi \le 1$ and separates the physical clock parameter ρ from the fractional-memory order α.

Let $L_j(\xi) = P_j(2\xi - 1)$ denote the shifted Legendre polynomial of degree j, where P_j is the classical Legendre polynomial. Its explicit representation is

$$L_j(\xi) = \sum_{k=0}^{j} a_{jk}\xi^k, \qquad a_{jk} = (-1)^{j+k}\frac{(j+k)!}{(j-k)!(k!)^2}. \tag{8}$$

The basis is orthogonal on the unit interval:

$$\int_0^1 L_i(\xi)L_j(\xi)\,d\xi = \frac{\delta_{ij}}{2j+1}. \tag{9}$$

Thus, a square-integrable function g may be approximated by $g_m(\xi) = C^T\Psi(\xi)$, where $\Psi(\xi) = [L_0(\xi), L_1(\xi), \ldots, L_m(\xi)]^T$. The coefficient formula $c_j = (2j+1)\int_0^1 g(\xi)L_j(\xi)d\xi$ also supplies the projection used below.

4.2. **Generalized-Caputo operational matrix.** To construct the operational matrix without the index ambiguities in the original formulation, define $q(\xi) = [1, \xi, \ldots, \xi^m]^T$ and the lower-triangular coefficient matrix $\mathcal{A} = (a_{jk})$, so that $\Psi(\xi) = \mathcal{A}q(\xi)$. For $k \ge 1$, the Caputo derivative of a monomial is

$$D_{0+}^{C,\alpha}\xi^k = \frac{\Gamma(k+1)}{\Gamma(k+1-\alpha)}\xi^{k-\alpha}, \quad k \ge 1; \qquad D_{0+}^{C,\alpha}1 = 0. \tag{10}$$

The noninteger power $\xi^{(k-\alpha)}$ is projected onto the first m+1 shifted-Legendre polynomials. If $h_{k\ell}$ denotes the coefficient of L_ℓ in this projection, orthogonality and Equation (8) give

$$h_{k\ell} = (2\ell+1)\sum_{r=0}^{\ell}\frac{a_{\ell r}}{k-\alpha+r+1}. \tag{11}$$

Define $\mathcal{G}_\alpha = (g_{k\ell})$ by $g_{0\ell} = 0$ and $g_{k\ell} = [\Gamma(k+1)/\Gamma(k+1-\alpha)]\,h_{k\ell}$ for $k \ge 1$. The order-(m+1) operational matrix is then

$$D_{0+}^{C,\alpha}\mathbf{\Psi}(\xi) \approx \mathcal{D}_\alpha\mathbf{\Psi}(\xi), \qquad \mathcal{D}_\alpha = \mathcal{A}\mathcal{G}_\alpha. \tag{12}$$

Because $\tau = T\xi$, differentiation with respect to transformed time contributes the scaling $T^{(-\alpha)}$. Hence ${}^C D_{0+}^\alpha \Psi(\tau/T) \approx T^{(-\alpha)}\mathcal{D}_\alpha\Psi(\tau/T)$. The first row associated with the constant basis function

is zero, as required by the Caputo derivative. This matrix form is algebraically equivalent to term-wise differentiation and projection, but it is easier to implement and audit than the multi-index expression used in the original paper.

4.3. **Spectral approximation of the fractional Brusselator.** For the homogeneous verification problem, the two transformed-time fields are approximated by

$$U_m(\tau) = \mathbf{C}^T\mathbf{\Psi}(\tau/T), \qquad V_m(\tau) = \mathbf{D}^T\mathbf{\Psi}(\tau/T). \tag{13}$$

where $C = [c_0, \ldots, c_m]^T$ and $D = [d_0, \ldots, d_m]^T$ contain 2(m+1) unknown coefficients. Substitution into the transformed Brusselator equations defines the residuals

$$R_u(\tau) = T^{-\alpha}\mathbf{C}^T\mathcal{D}_\alpha\mathbf{\Psi} - \Big[A - (B+1)U_m + U_m^2V_m\Big]. \tag{14a}$$

$$R_v(\tau) = T^{-\alpha}\mathbf{D}^T\mathcal{D}_\alpha\mathbf{\Psi} - \Big[BU_m - U_m^2V_m\Big]. \tag{14b}$$

Let ξ_i, $i = 1, \ldots, m$, be the m roots of $L_m(\xi)$, and let $\tau_i = T\xi_i$. Enforcing $R_u(\tau_i) = R_v(\tau_i) = 0$ supplies 2m collocation equations. The remaining two equations impose the initial data exactly:

$$\mathbf{C}^T\mathbf{\Psi}(0) = u_0, \qquad \mathbf{D}^T\mathbf{\Psi}(0) = v_0. \tag{15}$$

Equations (14)–(15) therefore form a square nonlinear system of $2(m+1)$ equations for $2(m+1)$ coefficients. This count corrects the ambiguity in the original description, which referred to both 2m collocation points and $2(m+1)$ equations without separating residual conditions from initial conditions.

4.4. **Singularity-adapted approximation.** Fractional solutions generally possess a weak initial expansion in powers of τ^α. An ordinary polynomial basis therefore converges more slowly near $\tau = 0$. The enriched approximation used in this study is

$$U_m(\tau) = u_0 + \tau^\alpha \sum_{j=0}^{m-1} c_j L_j(\tau/T), \qquad V_m(\tau) = v_0 + \tau^\alpha \sum_{j=0}^{m-1} d_j L_j(\tau/T). \tag{16}$$

The initial conditions are automatic, leaving 2m unknown coefficients and 2m residual conditions at the m shifted-Gauss nodes. Moreover, Equation (8) permits exact term-wise differentiation:

$$D_{0+}^{C,\alpha}\Big[\tau^\alpha L_j(\tau/T)\Big] = \sum_{k=0}^{j} a_{jk}T^{-k}\frac{\Gamma(\alpha+k+1)}{\Gamma(k+1)}\tau^k. \tag{17}$$

The right-hand side is an ordinary polynomial in τ. The enrichment therefore removes the dominant endpoint singularity from the approximation problem and explains the accuracy improvement quantified later in Figure 3 and Table 4.

4.5. **Nonlinear solution, residual assessment, and implementation.** The coefficient system is solved using a damped Newton or nonlinear least-squares method. A continuation strategy is used when necessary: the solution at a lower degree, or at a nearby fractional order, initializes the next calculation. All constants entering a high-precision solve are generated at the requested working precision; machine-precision numbers are not mixed with arbitrary-precision residual equations. This precaution avoids a warning that is encountered when decimal collocation nodes are supplied to a 40-digit calculation. Accuracy is evaluated independently of the collocation equations. On a dense validation grid, the differential residual norm is

$$E^R = \max_{0\le\tau\le T} \left\{ \left|R_u(\tau)\right|, \left|R_v(\tau)\right| \right\}. \tag{18}$$

and, when an independent reference solution is available, the maximum solution error is $E^s = \max\ \tau \left|U_m - U_{ref}\right|, \left|V_m - V_{ref}\right|$. The Jacobian condition number is reported alongside these errors because a small collocation residual alone does not guarantee an accurate or well-conditioned solution. The implementation is verified below against Runge–Kutta, fractional Adams–Bashforth predictor–corrector, and implicit L1 calculations.

5. Numerical Verification of the Homogeneous Model

5.1. **Integer-order benchmarks and spectral convergence.** The solution error decreases from 1.60×10^{-4} at degree 4 to 6.90×10^{-13} at degree 16, after which it reaches the reference and floating-point floor. The dense residual continues to decrease, whereas the Jacobian condition number grows from 13.9 to approximately 700 over the tested range. Reporting both error and conditioning prevents residual minimization from being mistaken for unlimited solution accuracy. Figure 1 confirms agreement with the benchmark trajectories, while Table 2 and Figure 2 quantify the associated degree of convergence, residual reduction, and conditioning cost.

Table 2 quantifies rapid convergence through degree 16: the maximum error falls by more than eight orders of magnitude from $m = 4$ to $m = 16$. The simultaneous increase in Jacobian conditioning explains why a still higher degree does not provide unlimited practical accuracy. Figure 1 presents the integer-order concentration profiles obtained with the shifted-Legendre collocation method. For $A = 0$ and $B = 1$, $u(t)$ decreases while $v(t)$ increases over the considered interval. For $A = 0.5$ and $B = 0.1$, $u(t)$ increases while $v(t)$ decreases. These monotonic profiles provide basic test cases for assessing numerical implementation. Quantitative agreement with the independent benchmark solution is evaluated using the errors and residuals reported in Table 2.

Figure 2 reveals an exponential-like error decay across the useful spectral range, followed by a numerical floor, while the condition number increases with degree. The combined trend indicates that increasing degrees beyond about 16 adds conditioning cost without a commensurate improvement in solution accuracy.

5.2. **Cross-method verification.** The fractional solution is independently checked using the Adams predictor–corrector method and an implicit L1 discretization. The three methods have

TABLE 2. Degree refinement for the integer-order benchmark.

Degree m	Maximum error	Dense residual	Jacobian condition
4	1.600e-04	4.678e-03	13.85
6	2.760e-06	1.104e-04	30.59
8	7.212e-08	6.297e-06	56.13
10	2.155e-09	2.261e-07	91.66
12	3.800e-11	4.067e-09	138.20
16	6.899e-13	9.048e-12	268.09
20	7.047e-13	6.840e-15	452.63
24	7.048e-13	1.665e-15	699.51

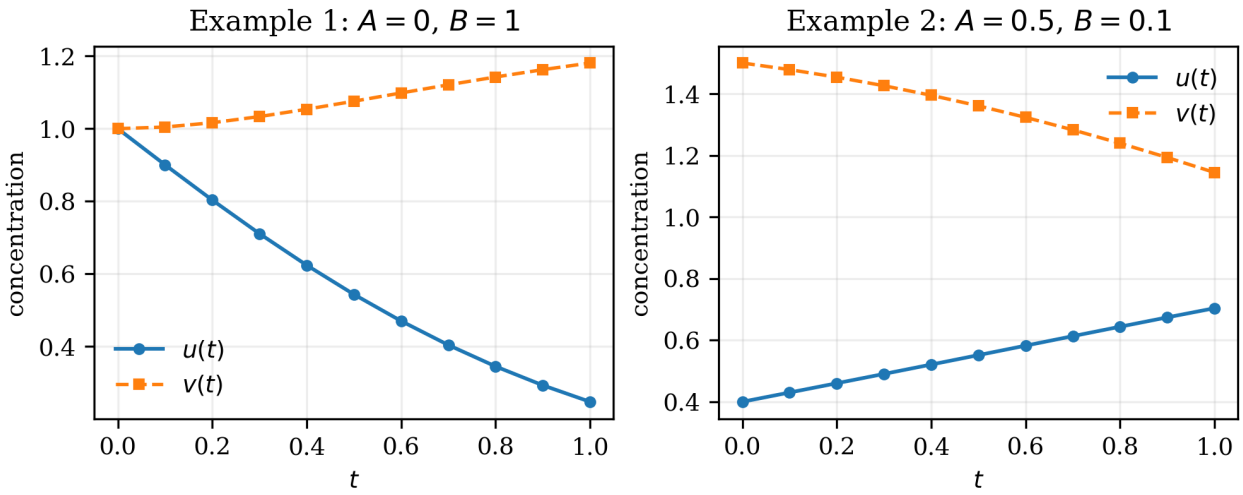


FIGURE 1. Integer-order solutions $u(t)$ and $v(t)$ for two parameter sets: (a) $A = 0$, $B = 1$, and (b) $A = 0.5$, $B = 0.1$, computed using the shifted-Legendre collocation method.

different approximation structures: global polynomial collocation, explicit history quadrature, and implicit convolution. The agreement, therefore, provides a stronger check than refinement of a single implementation. The Adams error decreases from 1.81×10^{-5} to 2.27×10^{-6} as the step count rises from 250 to 1000. The L1 method is more diffusive for this test but converges monotonically. Ordinary Legendre collocation is competitive for smooth cases but loses efficiency near the fractional endpoint singularity. The numerical comparison is reported in Table 3. Table 3 shows consistent convergence of two independent history-based solvers toward the collocation reference. Adams predictor–corrector is more accurate and faster for the tested grids, whereas the larger L1 error is consistent with its stronger numerical diffusion at comparable resolution.

5.3. **Endpoint enrichment and generalized-clock verification.** At degree 16, the enriched basis improves the tested fractional solutions by factors ranging from tens to 325. The advantage

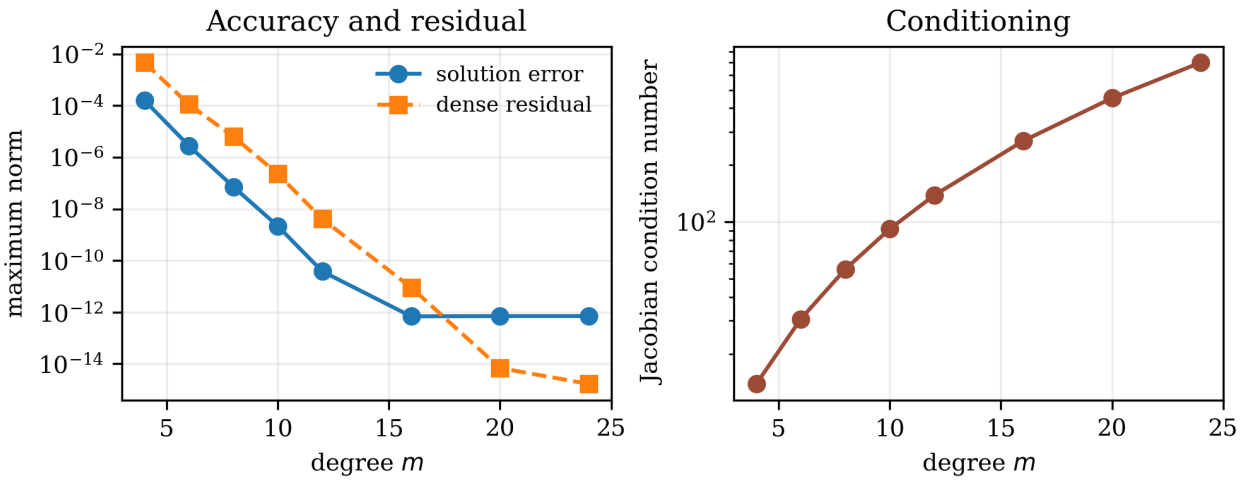


FIGURE 2. Spectral convergence, dense residual, and growth of nonlinear-system conditioning.

TABLE 3. Independent fractional-method comparison.

Method	Degrees/steps	Maximum error	Runtime (s)
Adams PC	250	1.805e-05	0.0089
Implicit L1	250	3.003e-03	0.1197
Adams PC	500	6.485e-06	0.0213
Implicit L1	500	1.784e-03	0.2343
Adams PC	1000	2.273e-06	0.0578
Implicit L1	1000	1.061e-03	0.4908
Legendre collocation	34	2.866e-03	0.0177

increases as the ordinary polynomial basis struggles to resolve the noninteger initial power. The exact clock transformation is verified separately: solutions obtained for different ρ values collapse when expressed in τ, to numerical precision. Figure 3 and Table 4 show the order-dependent gain from endpoint enrichment, and Figure 4 verifies the separate generalized-clock transformation. Figure 3 shows that the singularity-adapted basis outperforms the ordinary polynomial basis for every tested fractional order. The widening separation at the stronger endpoint singularity supports matching the approximation space to the expected fractional-time regularity. Table 4 quantifies the value of endpoint enrichment: the improvement factor rises from 27.6 at $\alpha = 0.50$ to a maximum of about 325 among the tested cases. These gains show that basis choice, rather than polynomial degree alone, controls efficiency for weakly singular fractional solutions. Figure 4 distinguishes an apparent change in physical-time evolution from a genuine change in state-space dynamics. Collapse in transformed time confirms that ρ rescales the clock, so it should not be interpreted as an independent kinetic or geological-memory parameter.

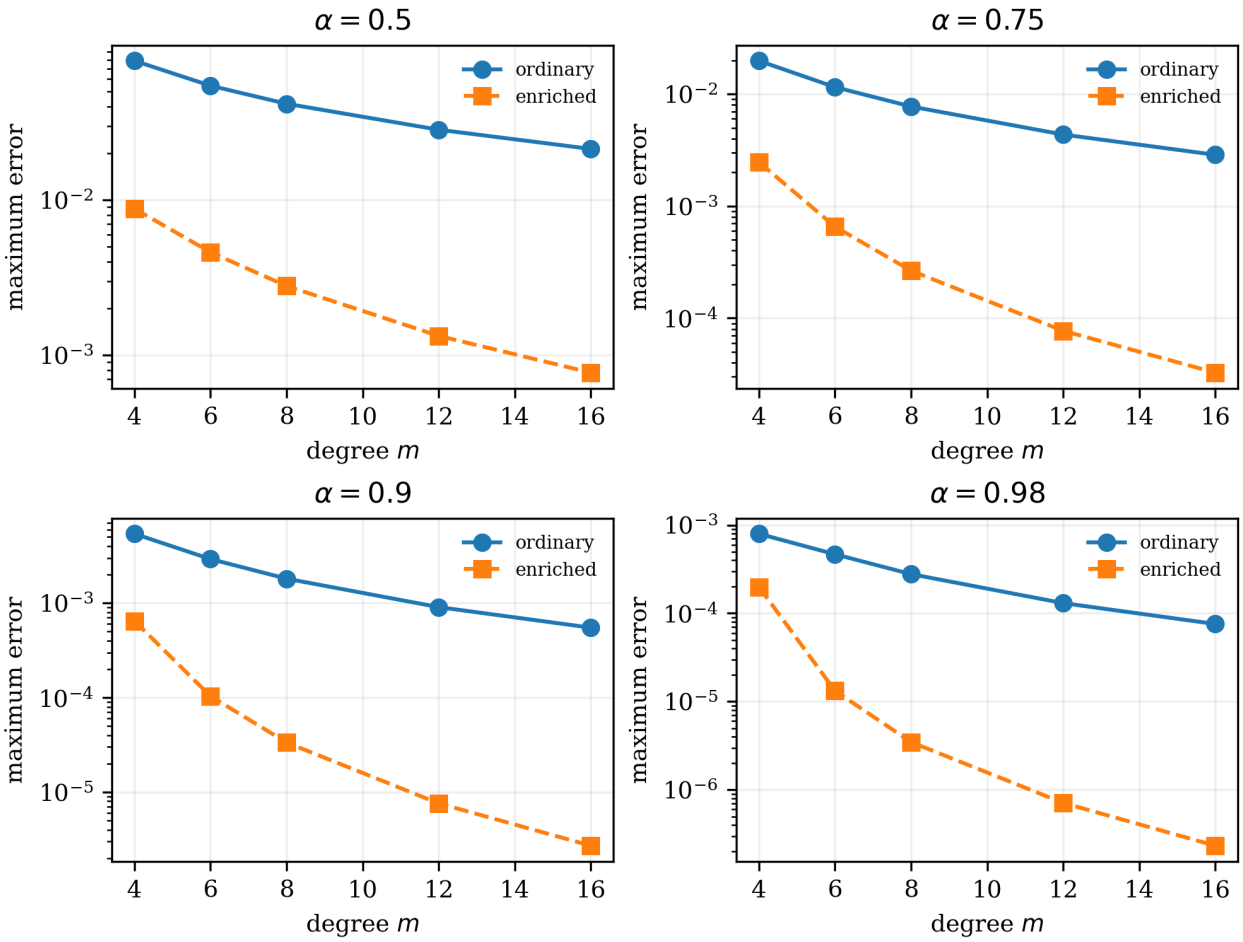


FIGURE 3. Ordinary and singularity-adapted shifted-Legendre errors for four fractional orders.

TABLE 4. Degree-16 improvement from endpoint enrichment.

α	Ordinary error	Enriched error	Improvement factor
0.50	2.130e-02	7.717e-04	27.6
0.75	2.866e-03	3.259e-05	87.9
0.90	5.489e-04	2.711e-06	202.5
0.98	7.571e-05	2.329e-07	325.0

6. Hydrothermal Numerical Method and Experimental Design

Centered second-order differences on a uniform grid approximate the spatial derivatives. Ghost-point reflection enforces the zero-flux boundaries. The resulting method-of-lines system is integrated in τ with the fractional Adams predictor–corrector algorithm of Diethelm, Ford, and Freed [15]. At each history step, the nonlinear reaction, precipitation, and porosity-dependent transport terms are evaluated consistently.

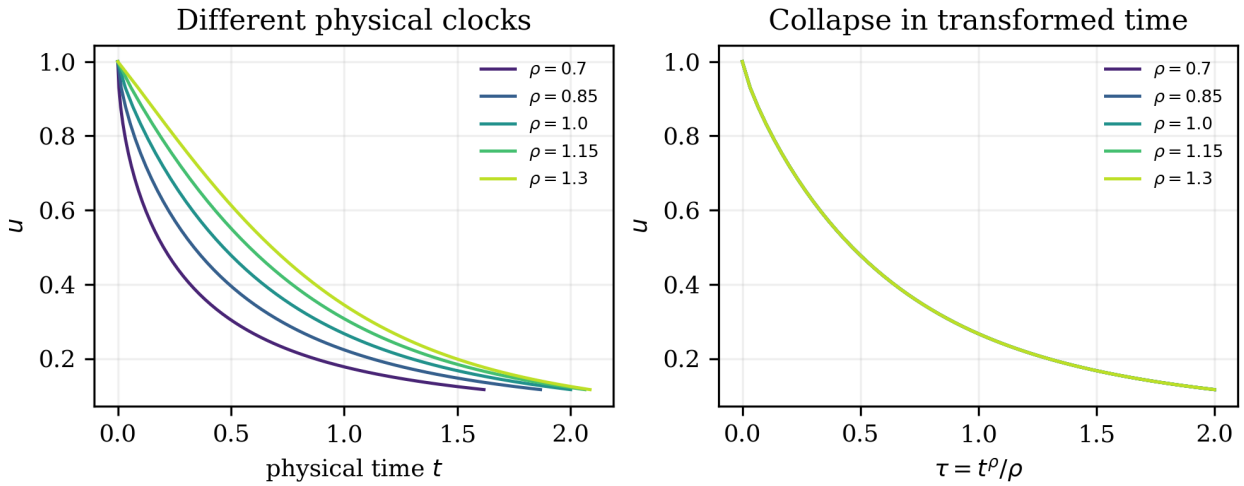


FIGURE 4. Generalized-clock verification for the homogeneous system. Physical-time curves differ, but the transformed trajectories collapse.

The algorithm retains the full Caputo history. For $n = 0, \ldots, N-1$, predictor weights are $b_j, n+1 = (n+1-j)^{\alpha} - (n-j)^{\alpha}$, followed by the standard Adams–Moulton corrector weights. Concentrations and precipitate are constrained only against small negative roundoff after each corrector step. Four controlled studies are performed: $\alpha \in 0.70, 0.85, 1.00$; $B \in 1.6, 2.0, 2.4, 2.8$; $k_p \in 0.01, 0.02, 0.03, 0.05$; and coupled versus fixed transport. The refinement sequence uses $(N_x, N_t) = (41, 240), (61, 360)$, and $(81, 480)$. All other parameters remain fixed so that individual effects are identifiable. Table 5 defines a deliberately controlled baseline in which one parameter group is varied at a time. This design isolates memory, forcing, precipitation, and clogging effects, although the dimensionless values should not be treated as site-calibrated hydrothermal properties.

TABLE 5. Dimensionless hydrothermal baseline configuration.

Quantity	Value	Quantity	Value
A	1.0	B	2.4
α	0.85	ρ	1.0
D_u	2×10^{-5}	D_v	1×10^{-4}
k_p	0.030	Ωc	1.80
φ_0	0.22	χ	0.055
T	12	grid	61×361

7. HYDROTHERMAL APPLICATION RESULTS

At T=12, the baseline mean precipitate is 0.1569; the maximum local precipitate is 0.1955. The minimum porosity decreases from 0.2200 to 0.2093. The spatially averaged permeability ratio is 0.8676, while its local minimum is 0.8372. The predicted heterogeneity, therefore, appears more

strongly in the local extreme than in the domain average. Figure 5 shows where and when these domain-scale and local responses develop. Figure 5 shows that a small initial spatial perturbation evolves into modulated reactant fields and nonuniform cumulative precipitation. Because precipitation is irreversible, transient chemical differences persist as mineral and permeability contrasts even after the mobile fields become smoother.

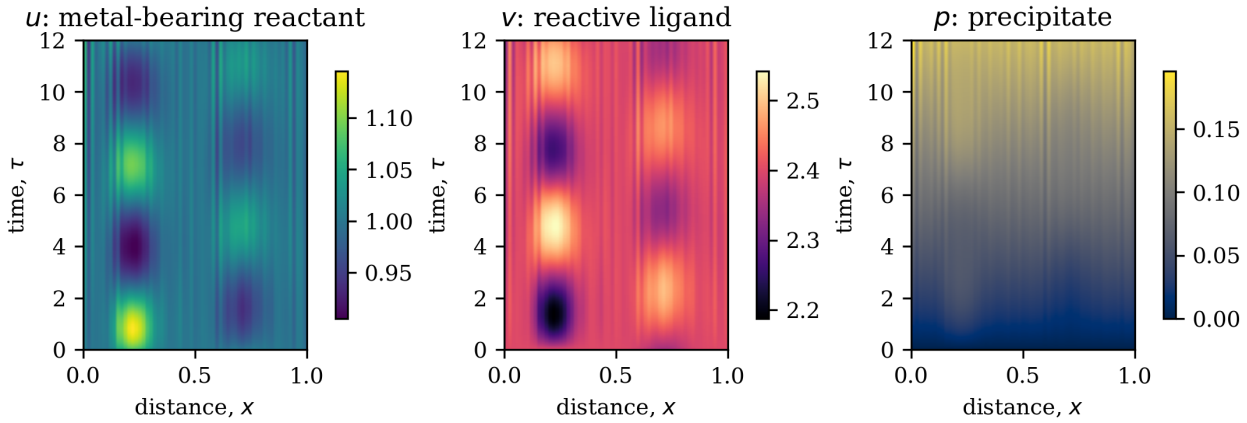


FIGURE 5. Baseline spatiotemporal hydrothermal fields for $\alpha = 0.85$, A=1, and B=2.4. Small initial heterogeneity evolves into temporally modulated reactant fields and spatially localized cumulative precipitation.

The integer-order case retains the largest late-time amplitude and deposits the most mineral. Relative to $\alpha = 1$, $\alpha = 0.70$ reduces final mean precipitation by 48.7%. This is a finite-time memory effect, not proof that fractional behavior always lowers ultimate mineral yield; longer simulations and calibrated orders are needed to establish asymptotic consequences. Figure 6 displays the trajectories, and Table 6 quantifies the terminal hydraulic and precipitation consequences. Figure 6 demonstrates progressive damping and delayed accumulation as α decreases. The result links stronger fractional memory to weaker late-time oscillations and lower finite-window mineral yield under the stated parameter set, without implying a universal reduction at infinite time. Table 6 shows a monotonic increase in late-time oscillation amplitude and mean precipitate as α approaches unity, accompanied by lower minimum porosity and permeability. The hydraulic columns demonstrate that the chemical memory effect propagates into a measurable sealing response.

TABLE 6. Influence of fractional order at T=12.

α	Late $\Delta\bar{u}$	Mean p	Minimum φ	Minimum k/k_0
0.70	0.00149	0.1127	0.2125	0.8835
0.85	0.01970	0.1569	0.2093	0.8372
1.00	0.12807	0.2199	0.2048	0.7762

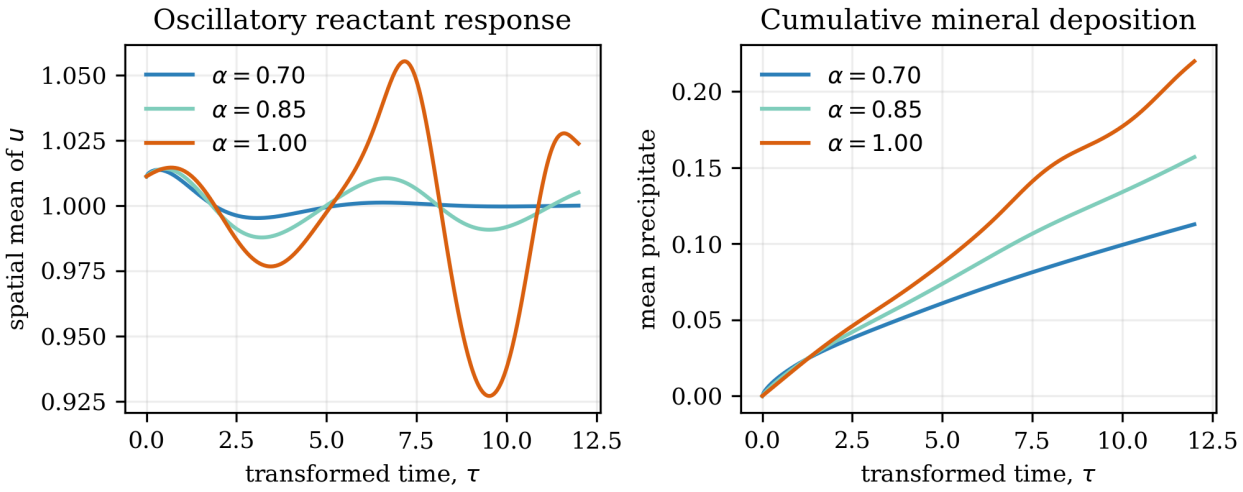


FIGURE 6. Fractional-order comparison. Lower α damps the spatially averaged reactant oscillation and reduces cumulative precipitation over the fixed transformed-time interval.

Below the classical Hopf threshold, $B = 1.6$, yields essentially no precipitation because the reaction flux rarely exceeds Ω_c. At B=2.8, the final mean precipitate reaches 0.2655, and the most clogged location loses 37.9% of its initial permeability. The transition is controlled jointly by the Brusselator instability and the imposed precipitation threshold. The full forcing sweep is visualized in Figure 7 and summarized numerically in Table 7.

Mean mineral accumulation is nearly proportional to k_p over this range. The constitutive transformation is nonlinear: at $k_p = 0.05$, mean permeability loss is 21.3%, and the maximum local loss is 25.4%. This trade-off is directly relevant to hydrothermal sealing and to engineered in-situ leaching, where reaction yield and sustained injectivity compete. The right-hand panels of Figure 7 and the values in Table 8 demonstrate this yield–clogging trade-off. Figure 7 separates two controls on mining-relevant behavior: B governs whether the nonlinear reaction repeatedly crosses the precipitation threshold, whereas k_p mainly scales how rapidly those exceedances become solid accumulation. Both stronger forcing and faster precipitation increase sealing, but through different mechanisms. Table 7 identifies a threshold-like change across the B sweep: deposition is negligible at B=1.6 but grows rapidly above the classical Hopf threshold. The concurrent rise in maximum permeability loss indicates that nonlinear kinetic forcing can switch the modeled fracture from effectively open to substantially clogged. Table 8 shows nearly proportional growth of mean precipitate with k_p over the tested range, but a nonlinear increase in permeability loss through the porosity–permeability closure. Thus, mineral yield and hydraulic damage should be evaluated jointly in any mining or injection scenario.

For the selected effective transport coefficients, porosity feedback changes the domain-mean precipitate by less than 0.1%, although it modifies local precipitation and permeability profiles. This small difference is itself informative: the baseline lies in a reaction-dominated regime. Stronger

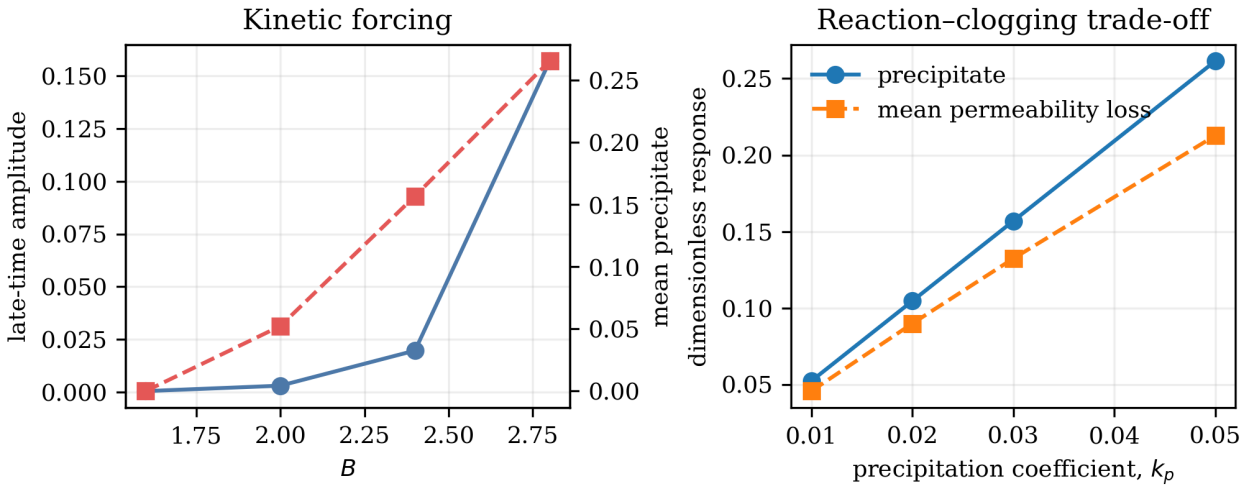


FIGURE 7. Comparative parameter studies. Left: increasing B amplifies the nonlinear response and precipitation. Right: increasing k_p raises mineral accumulation and permeability loss.

TABLE 7. Kinetic forcing swept at $\alpha = 0.85$.

B	Late $\Delta\bar{u}$	Mean p	Maximum permeability loss
1.6	0.00049	0.00002	0.0%
2.0	0.00306	0.05231	5.1%
2.4	0.01970	0.15689	16.3%
2.8	0.15699	0.26548	37.9%

TABLE 8. Precipitation-rate and clogging comparison.

k_p	Mean p	Minimum φ	Mean k loss	Maximum k loss
0.010	0.0523	0.2163	4.6%	5.8%
0.020	0.1046	0.2127	9.0%	11.2%
0.030	0.1569	0.2093	13.2%	16.3%
0.050	0.2614	0.2025	21.3%	25.4%

dispersion, longer time, larger χ, or an explicit advective flux would increase transport–clogging feedback. The near-overlap of the terminal precipitation profiles in Figure 8 confirms the weak domain-average feedback under the baseline conditions. Figure 8 shows only a small separation between coupled- and fixed-transport precipitation profiles, consistent with a reaction-dominated baseline. In contrast, the porosity and permeability curves make the localized hydraulic consequence clear: modest solid accumulation can produce a more pronounced transmissivity reduction.

The mean precipitate varies by at most 0.048% across the tested grids (the coarsest and finest values themselves differ by only 0.0045%; the largest spread involves the intermediate resolution), and the mean permeability differs by 0.020% between the coarsest and finest grids. Local maxima converge more slowly because the initial perturbation contains grid-scale heterogeneity; conclusions are therefore based primarily on spatially integrated quantities. Table 9 demonstrates that the domain-mean precipitate and permeability estimates are stable under simultaneous spatial and temporal refinement. The slower stabilization of the late-time amplitude supports using integrated mineral and hydraulic measures as the primary quantitative outputs.

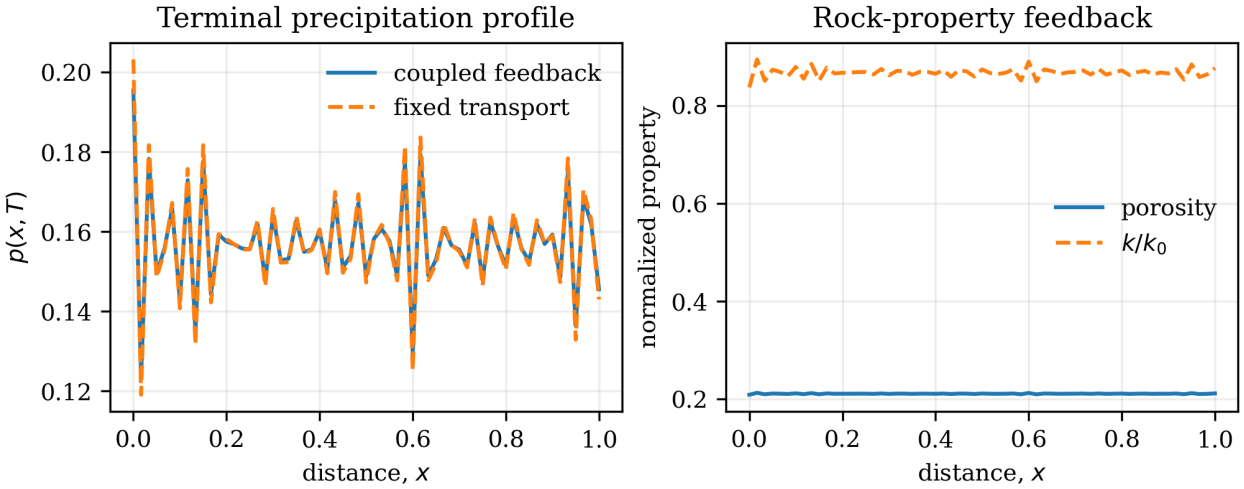


FIGURE 8. Terminal profiles for the baseline case. Left: precipitation with coupled and fixed transport. Right: porosity and normalized permeability under the coupled closure.

TABLE 9. Spatial and temporal refinement.

N_x	N_t	Mean p	Mean k/k_0	Late $\Delta\bar{u}$
41	240	0.156962	0.867528	0.019467
61	360	0.156893	0.867620	0.019704
81	480	0.156969	0.867698	0.019133

The clock-collapse experiment prevents an important interpretive error. A fitted value of ρ does not independently quantify reaction strength, ore grade, or transport heterogeneity. It only maps transformed time to physical time. Geological memory is represented by α, subject to empirical validation. Figure 9 provides the direct physical-time and transformed-time comparison. Figure 9 shows different apparent rates when the results are plotted against physical time, but exact superposition against τ. This collapse is a diagnostic check on the implementation and prevents ρ-driven time stretching from being mistaken for changes in ore-forming intensity.

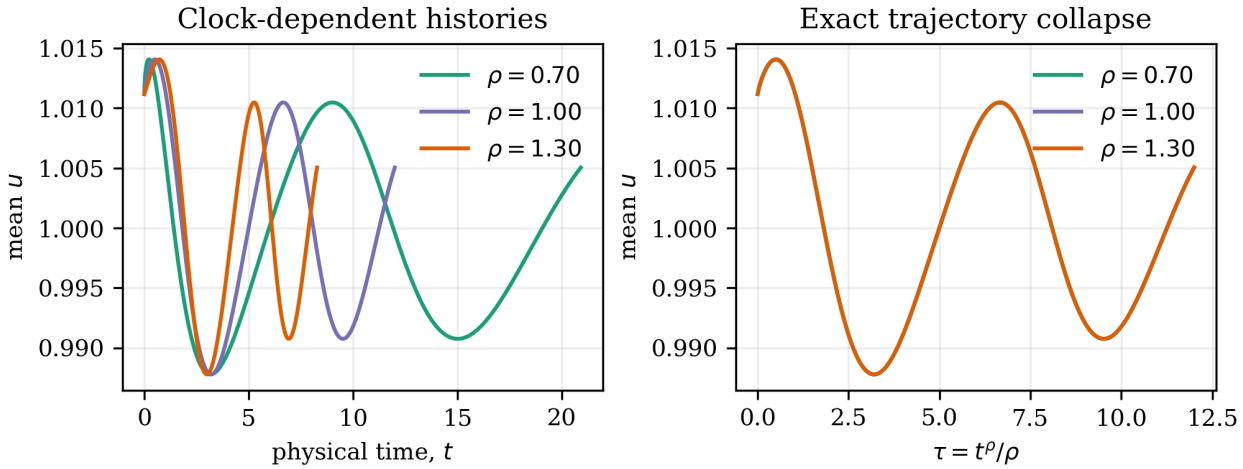


FIGURE 9. Effect of ρ in the hydrothermal system. Curves differ in physical time t but collapse exactly when plotted against $\tau = t^{\rho}/\rho$.

8. Geophysical and Mining Implications

Oscillatory reactant histories can produce pulses of supersaturation and mineral growth. In a moving fluid or a growing vein, temporal oscillations may be recorded as spatial bands. The present stationary one-dimensional model demonstrates the chemical mechanism but does not convert time directly to vein-growth distance. Such a comparison would require a growth velocity and petrographic age or band-spacing data. The precipitation–porosity closure converts reaction history into a hydraulic consequence. The B and k_p sweeps identify conditions ranging from negligible alteration to substantial local permeability loss. This makes the framework useful for qualitative studies of vein sealing, geothermal scaling, and loss of injectivity during reactive fluid circulation. For in-situ leaching, u and v may be reinterpreted as an effective lixiviant–metal reaction pair and p as an undesirable secondary precipitate. The model then poses a practical competition: stronger chemistry can improve dissolution or conversion while accelerating pore blockage. A mining application must add advection, reversible mineral reactions, sorption, and a recovery function at the production boundary. Table 10 emphasizes that the present equations are a transferable conceptual core rather than a field-ready predictor. Each target application requires distinct observations and added physics; in particular, mining deployment needs flow, recovery, and mineral-specific reaction data before operational decisions can be supported.

9. Limitations and Validation Requirements

The present results are dimensionless and synthetic. They demonstrate mathematical behavior, not a prediction for a named ore deposit. The following limitations must be resolved before geological inference:

- The two Brusselator variables do not enforce elemental mass balance, charge balance, or aqueous speciation.

TABLE 10. Route from the present conceptual model to field application.

Target	Required observations	Necessary extension
Hydrothermal vein zoning	Band spacing, mineral sequence, fluid inclusions	Growth/advection mapping and mineral-specific kinetics
Geothermal scaling	Fluid chemistry, temperature, scale mass, and injectivity	Thermal coupling and calibrated saturation indices
In-situ leaching	Injection/production histories, recovery, permeability	Advection, dissolution, sorption, and well boundaries
Acid mine drainage	Fe/S speciation, pH, redox, discharge	Charge balance, microbial kinetics, aqueous speciation

- Temperature, pressure, pH, and redox potential are implicit in A, B, and the precipitation threshold.
- Effective diffusion replaces advective fracture flow and matrix exchange.
- A common fractional order is assumed for all state variables.
- Kozeny–Carman's behavior may be inappropriate for an opening or closing fracture.
- Parameter identifiability has not been tested against observations.

A defensible validation sequence would first fit α and transport parameters to conservative-tracer breakthrough curves, then fit reaction and precipitation parameters to laboratory flow-through data, and finally test permeability and mineral-volume predictions against independent measurements. Competing integer-order, multirate-mass-transfer, and continuous-time-random-walk models should be compared using out-of-sample criteria rather than fit quality alone.

10. Conclusions

This study presented the fractional Brusselator as a reduced model of oscillatory mineral precipitation in a hydrothermal fracture. The essential advance is not a claim that the Brusselator reproduces a particular ore-forming reaction. Rather, it is the construction of a transparent bridge between nonlinear reaction dynamics and geologically persistent consequences. Two mobile reaction coordinates are transported along a one-dimensional domain; their nonlinear interaction generates a supersaturation proxy, accumulated precipitate reduces porosity, and the evolving pore structure modifies effective transport. In this form, the model can test mechanistic hypotheses about episodic mineral growth and fracture sealing while remaining simple enough for bifurcation analysis and controlled parameter studies.

The fractional-order comparison establishes a clear finite-time memory effect. At T=12, reducing α from 1.00 to 0.70 lowers the spatially averaged precipitate from 0.2199 to 0.1127, a decrease of 48.7%, while the late-time reactant amplitude falls from 0.12807 to 0.00149. Thus, under the selected forcing and observation window, stronger memory smooths the oscillatory response and

delays cumulative deposition. This result should be interpreted as a model-dependent transient statement. Fractional dynamics may alter phase, decay, and long-time behavior differently in other parameter regimes; the present calculations do not establish a universal monotonic relation between α and ultimate ore volume.

The kinetic-forcing study shows that the precipitation threshold converts the Brusselator transition into a sharp geological response. At B=1.6, below the classical Hopf threshold for A=1, mean deposition is approximately 2×10^{-5}, and permeability remains essentially unchanged. At B=2.8, the mean precipitate rises to 0.2655, and the most affected location loses 37.9% of its initial permeability. The result demonstrates how a modest change in a lumped kinetic control can separate an open, weakly altered pathway from a strongly mineralized and partially sealed pathway. In a real system, B would have to be related to measurable feed composition, temperature, redox state, or reaction-rate ratios before such a transition could be used predictively.

The precipitation-rate sweep identifies a second, more gradual trade-off. Increasing k_p from 0.01 to 0.05 raises mean precipitate from 0.0523 to 0.2614 and increases mean permeability loss from 4.6% to 21.3%. This behavior is relevant both to natural vein sealing and to mining operations. In geothermal circulation or in-situ leaching, stronger chemical conversion may be desirable, but accelerated secondary precipitation can reduce injectivity, redirect flow, and isolate recoverable material. The coupled model provides a compact way to map this competition before introducing a more expensive multicomponent simulator.

The generalized derivative parameters have distinct interpretations. The order α controls the nonlocal memory kernel and changes stability and reaction history. In contrast, the identity $\tau = t^{\rho}/\rho$ proves that ρ is an exact clock transformation for the operator used here. Curves that appear different in physical time collapse in transformed time. Consequently, ρ must not be reported as an independent measure of ore-forming intensity, heterogeneity, or reaction strength. This separation is important for parameter estimation and is one of the main analytical conclusions of the work.

The numerical evidence supports the integrated comparisons. Across the refinement sequence, the mean precipitate varies by at most 0.048% and the mean permeability by 0.020% between the coarsest and finest calculations. Local extrema converge more slowly because the imposed initial heterogeneity contains short spatial scales. The study, therefore, bases its quantitative conclusions on domain-integrated measures and treats maximum local clogging as a resolution-sensitive diagnostic. The coupled and fixed-transport cases differ only slightly in mean deposition for the baseline coefficients, indicating a reaction-dominated regime rather than a strongly transport-limited one.

Several geological conclusions follow, but all remain hypotheses until calibrated. Autonomous nonlinear chemistry can generate repeated supersaturation pulses without externally periodic forcing; mineral accumulation can transform temporary chemical oscillations into permanent zoning; and sufficiently strong precipitation can feed back on pathway transmissivity. These

mechanisms are plausible contributors to banded veins, hydrothermal sealing, geothermal scale formation, and secondary precipitation during in-situ leaching. They do not exclude pressure cycling, episodic fluid injections, fracture propagation, cooling, boiling, or externally driven redox changes.

The immediate next step is validation at the laboratory scale. Conservative-tracer experiments should first constrain residence-time behavior and test whether a fractional model outperforms integer-order dispersion, multirate mass transfer, or continuous-time-random-walk alternatives. Reactive flow-through experiments should then measure dissolved species, precipitated mass, spatial mineral distribution, porosity, and permeability simultaneously. Mineral-specific saturation indices and kinetic rate laws can replace the threshold term, while temperature, advection, matrix exchange, and evolving fracture aperture can be added sequentially. Parameters estimated from one experiment should be evaluated against an independent experiment to assess predictive, not merely descriptive, performance.

In summary, the presented framework is best regarded as a hypothesis-generating and benchmarking model. It extends a mathematical fractional oscillator into a coupled reaction–transport–precipitation system, identifies measurable consequences of memory and kinetic forcing, and states the conditions required for geological use. Its value lies in clarifying mechanisms and designing comparisons. Reliable prediction of a named hydrothermal deposit or mining operation will require thermodynamic consistency, elemental and charge conservation, calibrated kinetics, realistic hydraulic boundaries, uncertainty analysis, and field-scale verification.

Acknowledgements: The authors extend their appreciation to Northern Border University, Saudi Arabia, for supporting this work through project number (NBU-CRP-2026-1266).

Conflicts of Interest: The authors declare that there are no conflicts of interest regarding the publication of this paper.

References

[1] C.I. Steefel, D.J. DePaolo, P.C. Lichtner, Reactive Transport Modeling: An Essential Tool and a New Research Approach for the Earth Sciences, Earth Planet. Sci. Lett. 240 (2005), 539–558. https://doi.org/10.1016/j.epsl.2005.09.017.

[2] C.I. Steefel, M. Hu, Reactive Transport Modeling of Mineral Precipitation and Carbon Trapping in Discrete Fracture Networks, Water Resour. Res. 58 (2022), e2022WR032321. https://doi.org/10.1029/2022WR032321.

[3] Q. Zhang, H. Deng, Y. Dong, S. Molins, X. Li, et al., Investigation of Coupled Processes in Fractures and the Bordering Matrix via a Micro-Continuum Reactive Transport Model, Water Resour. Res. 58 (2022), e2021WR030578. https://doi.org/10.1029/2021WR030578.

[4] Z. Wang, M. Hu, C. Steefel, Pore-Scale Modeling of Reactive Transport with Coupled Mineral Dissolution and Precipitation, Water Resour. Res. 60 (2024), e2023WR036122. https://doi.org/10.1029/2023WR036122.

[5] B. Berkowitz, A. Cortis, M. Dentz, H. Scher, Modeling Non-Fickian Transport in Geological Formations as a Continuous Time Random Walk, Rev. Geophys. 44 (2006), RG2003. https://doi.org/10.1029/2005RG000178.

[6] Y. Edery, S. Geiger, B. Berkowitz, Structural Controls on Anomalous Transport in Fractured Porous Rock, Water Resour. Res. 52 (2016), 5634–5643. https://doi.org/10.1002/2016WR018942.

[7] A. Velásquez-Parra, T. Aquino, M. Willmann, Y. Méheust, T. Le Borgne, et al., Sharp Transition to Strongly Anomalous Transport in Unsaturated Porous Media, Geophys. Res. Lett. 49 (2022), e2021GL096280. https://doi.org/10.1029/2021GL096280.

[8] I. Prigogine, R. Lefever, Symmetry Breaking Instabilities in Dissipative Systems. II, J. Chem. Phys. 48 (1968), 1695–1700. https://doi.org/10.1063/1.1668896.

[9] J. Deng, R.P. Sharma, P. Szymczak, P.K. Kang, Anomalous Transport in Dissolving Porous Media: Transitions Between Fickian and Non-Fickian Regimes, Geophys. Res. Lett. 52 (2025), e2025GL115940. https://doi.org/10.1029/2025GL115940.

[10] U.N. Katugampola, A New Approach to Generalized Fractional Derivatives, Bull. Math. Anal. Appl. 6 (2014), 1–15.

[11] J. Hommel, E. Coltman, H. Class, Porosity–Permeability Relations for Evolving Pore Space: A Review with a Focus on (Bio-)geochemically Altered Porous Media, Transp. Porous Media 124 (2018), 589–629. https://doi.org/10.1007/s11242-018-1086-2.

[12] C. Canuto, M.Y. Hussaini, A. Quarteroni, T.A. Zang, Spectral Methods: Fundamentals in Single Domains, Springer, Berlin, Heidelberg, 2006. https://doi.org/10.1007/978-3-540-30726-6.

[13] J.P. Boyd, Chebyshev and Fourier Spectral Methods, second ed., Dover Publications, Mineola, New York, 2001.

[14] I. Podlubny, Fractional Differential Equations, Academic Press, San Diego, 1999.

[15] K. Diethelm, N.J. Ford, A.D. Freed, A Predictor-Corrector Approach for the Numerical Solution of Fractional Differential Equations, Nonlinear Dyn. 29 (2002), 3–22. https://doi.org/10.1023/A:1016592219341.